Journal of Computational Physics **180,** 1–24 (2002)
doi:10.1006/jcph.2001.6953

Numerical Methods for Multiple Inviscid Interfaces in Creeping Flows

M. C. A. Kropinski[1]

Department of Mathematics, Simon Fraser University, Burnaby, British Columbia, Canada V5A 1S6
E-mail: mkropins@cs.sfu.ca

Received November 3, 2000; revised September 4, 2001

We present new, highly accurate, and efficient methods for computing the motion of a large number of two-dimensional closed interfaces in a slow viscous flow. The interfacial velocity is found through the solution to an integral equation whose analytic formulation is based on complex-variable theory for the biharmonic equation. The numerical methods for solving the integral equations are spectrally accurate and employ a fast multipole-based iterative solution procedure, which requires only $O(N)$ operations where N is the number of nodes in the discretization of the interface. The interface is described spectrally, and we use evolution equations that preserve equal arclength spacing of the marker points. We assume that the fluid on one side of the interface is inviscid and we discuss two different physical phenomena: bubble dynamics and interfacial motion driven by surface tension (viscous sintering). Applications from buoyancy-driven bubble interactions, the motion of polydispersed bubbles in an extensional flow, and the removal of void spaces through viscous sintering are considered and we present large-scale, fully resolved simulations involving $O(100)$ closed interfaces.

Key Words: Stokes flow; fluid interfaces; integral equations; fast-multipole methods; multiply-connected domains.

1. INTRODUCTION

The motion of deformable interfaces in a slow viscous flow is a fundamental problem with relevance to a number of physical processes, including emulsion sedimentation and rheology, drop coalescence and breakup, and the viscous sintering phenomenon. Given the highly complicated nature of this type of problem, numerical simulation has become one of the most important tools for investigation. However, even with increased speed and memory, current computational architecture is still restricted, when not coupled with

[1] The work of this author was supported by NSERC grants WFA 0172672 and RGPIN 203326.

0021-9991/02 $35.00

modern fast algorithms, in its ability to handle large-scale problems with a high degree of accuracy.

In this paper, efficient methods are presented that can be used to accurately calculate the deformation of a large number of closed interfaces using only modest computational resources. These methods are an extension of those presented in [20] for investigating the motion of a single, closed interface in a Stokes flow. Here, we consider the case in which the fluid on one side of these interfaces is inviscid, and thus the interface boundaries represent bubbles or gas pockets in the flow. There are three novel elements to these methods. First, the governing fluid dynamics are described by an integral equation formulation which is solved using spectrally accurate, fast methods. Second, evolution equations are used that preserve equal arclength spacing of the marker points on the interface, thereby maintaining the mesh dynamically and preserving a low-order stability constraint. Third, in order to maintain a high degree of accuracy, the interface is described using a spectral mesh. We present several simulations which track up 70,000 marker points representing $O(100)$ bubbles or gas pockets.

To find solutions to the Stokes equations, the integral equation methods developed for a single closed interface in [20] are extended to those that are capable of handling multiply-connected bounded, unbounded, or semi-infinite (wall-bounded) domains. The starting point is the classical Sherman–Lauricella equation which has its analytic foundation in the complex variable theory for the biharmonic equation. As seen in [10] for the case of solid particles in a Stokes flow, a direct application of the integral equations for simply-connected problems will become rank deficient in multiply-connected domains. Here, the resolution of this rank deficiency is dependent on the nature of the problem under consideration and we separate our discussion into two cases: bubble dynamics and viscous sintering. The discretization of the integral equation is spectrally accurate and the fast multipole method [4, 8, 33] is used to compute the matrix–vector products in the iterative solution of the resulting linear system. With N points in the discretization of the boundary, our method requires only $O(N)$ operations, versus direct Gaussian elimination [38, 41] which are $O(N^3)$. Standard implementations of iterative schemes (c.f. [5, 29]) require $O(N^2)$ operations, thus limiting these studies to only modest-sized problems in the range of 20–40 drops or bubbles (an insufficient number to determine statistical properties of evolving microstructure [5], for example). Recently, Zinchenko and Davis [42] presented an economic multipole technique for large-scale simulations of three-dimensional drops. Their algorithm is $O(M^2P^{3/2})$, where M is the number of drops, P is the number of points per drop, and the prefactor on this operation count is small. For $M = O(100)$ and $P = O(1000)$, their method is quite efficient. While the accuracy of their calculations appears to be adequate, they do rely on artificial smoothing to supress numerical instabilities and to enable larger time steps to be taken. Also, it would be difficult in their formulation to introduce local adaptive refinement, if needed.

Here, the interface is described using a spectral mesh, with the number of points always being large enough to guarantee full spatial precision. More typical descriptions, such as cubic splines or polygonal approximations, can lead to underresolved features on the interface (for example, curvature). We demonstrate that this can introduce significant error during the course of a simulation. In addition, we follow the approach used in [20], which is to dynamically maintain equal arclength spacing of marker points on the interface. Other authors [14, 35, 43] have used this approach in various studies of interfacial motion, and we showed in [20] that this *equal arclength frame* can eliminate both the stiffness that can

arise when regions of high curvature develop (c.f. [38, 41]) and the need for prohibitively small explicit time steps when grid points are allowed to cluster in an adaptive fashion. Since the nature of the stability constraint is well understood in our simulations (it is equivalent to a CFL-type condition), we can guarantee our time stepping methods to be fully stable.

We consider only two-dimensional problems. While certain physical effects are lost in this reduction of dimension, it has been noted by many authors (see the discussions in [5, 21] for example) that two-dimensional bubbles and drops retain enough of the qualitative features seen in three dimensions to maintain a high degree of physical relevance. We note that the fast multipole method is available in three dimensions [11, 12], which could be incorporated, in the future, into a primitive variable formulation for a three-dimensional study of the problems presented here.

In the next section, the governing equations for fluid interfaces in a Stokes flow are outlined. The discussion is separated into two problems: the first considers the motion of a viscous fluid filled with gas pockets being driven solely by surface tension and the second concerns the deformation of bubbles under the action of applied and hydrodynamic forces. In Section 3, the relevant complex variable theory for the biharmonic equation is briefly reviewed. This theory leads to the formulation of the integral equations in Section 4. In Section 5, our numerical methods are presented and several examples are given in Section 6.

2. PROBLEM FORMULATION

We consider the motion of a collection of closed fluid interfaces suspended in a two-dimensional slow viscous flow, with the fluid or gas contained within the interfaces being inviscid. The viscous fluid domain, then, is multiply-connected and may be finite, infinite, or semi-infinite (wall-bounded) in extent. The component boundaries are denoted by Γ_1, $\Gamma_2, \ldots, \Gamma_M$, and in the case of a bounded fluid domain, the outer boundary is described by Γ_0 (see Fig. 1). We let Γ represent the union of all such component curves.

We present the governing equations in their nondimensional form by choosing the characteristic length as the radius a of a typical bubble or void size, velocity as σ/μ, where σ is the surface tension and μ is the kinematic viscosity (assumed to be constant), time as $a\mu/\sigma$, and pressure as σ/a. We assume that the Reynolds number is small, thus the equations governing the fluid motion in D are the Stokes equations

$$\nabla^2 \mathbf{u} = \nabla p, \quad \nabla \cdot \mathbf{u} = 0, \quad \mathbf{x} \in D, \tag{1}$$

where $\mathbf{u} = (u, v, 0)$ is the velocity and p is pressure. Gravity effects, if included, have been absorbed into the pressure term through $p = \Pi - (\rho g a^2/\sigma)\mathbf{n_g} \cdot \mathbf{x}$, where ρ is the density of the fluid, Π is the dynamic pressure, and $\mathbf{n_g}$ is the unit normal pointing in the direction of gravity.

We now separate the discussion into two separate classes of problems, each representing different phenomena of interface motion. The first considers the motion of a viscous fluid filled with void spaces being driven solely by surface tension. This problem is entitled *viscous sintering*. We call the second class *bubble dynamics* as it is concerned with the deformation of bubbles under the action of applied and hydrodynamic forces.

Viscous Sintering. The motion of a viscous fluid driven solely by surface tension serves as one mechanism for sintering: a process by which void spaces or gas pockets are removed

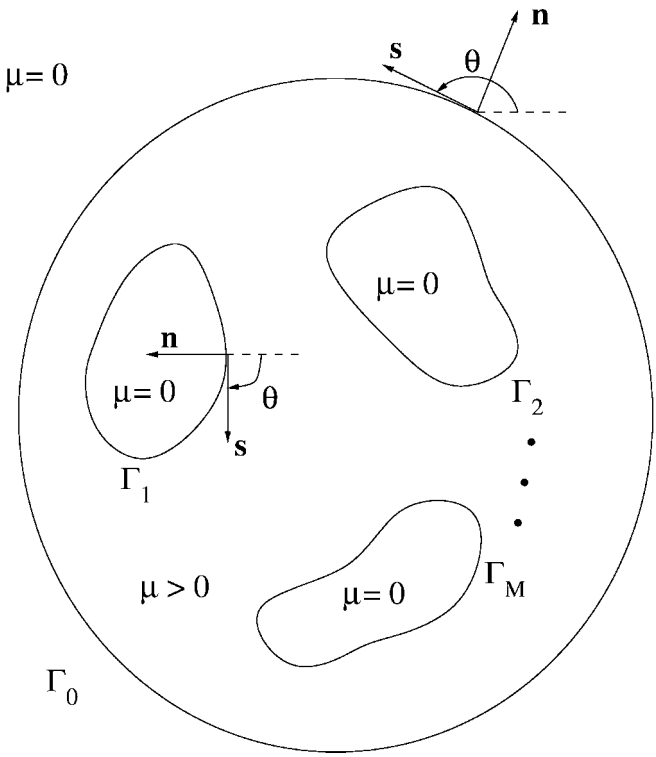

FIG. 1. A collection of bubbles/gas pockets in a bounded viscous fluid domain D. The unit normal $\mathbf{n}$ points out of D and θ is the tangent angle to Γ. The local curvature is given by $\kappa = \theta_s$, where s is arclength increasing in a clockwise direction on $\Gamma_1, \ldots, \Gamma_M$, and counterclockwise on Γ_0.

from a granular compact by heating. In this situation, the fluid domain is bounded and contains void spaces described by the component curves Γ_k, $k > 0$. Following the model as outlined in [30, 31, 38–41], the appropriate interface condition is that the normal component of stress is the product of surface tension and curvature. In nondimensional form, this is

$$\Sigma\mathbf{n} = -\kappa\mathbf{n}, \quad \mathbf{x} \in \Gamma. \tag{2}$$

(We assume a zero gas pressure inside of the void spaces [30, 31].) Here κ is the local curvature (see Fig. 1 for orientation), $\mathbf{n}$ is the outward pointing normal, and $\Sigma = -p\mathbf{I} + [\nabla\mathbf{u} + (\nabla\mathbf{u})^T]$ is the stress tensor.

Bubble Dynamics. In this second class of problems, we consider the motion and deformation of bubbles under the action of hydrodynamic forces and possibly gravity effects. In this case, we assume the fluid domain is unbounded or wall-bounded and the component curves Γ_k represent the bubble boundaries. We assume also that the bubbles contain a perfect gas, and that the bubble rise is small. Under these assumptions, the change in hydrostatic pressure is small compared to the ambient fluid pressure and we can further assume that the volume of each bubble remains constant [32]. In the case of a single bubble, the gas pressure inside is set arbitrarily to zero. If there is more than one bubble, each has its own value of internal gas pressure $p_k(t)$. The appropriate stress interface condition is

$$(\Sigma + p_k\mathbf{I})\mathbf{n} = -\kappa\mathbf{n} + \mathcal{B}\mathbf{n}_\mathbf{g} \cdot \mathbf{x}\,\mathbf{n}, \quad \mathbf{x} \in \Gamma. \tag{3}$$

Here $\mathcal{B}$ is the bond number,

$$\mathcal{B} = \frac{\Delta\rho g a^2}{\sigma},$$

where $\Delta\rho$ is the difference in density between the fluid and the gas in the bubble, respectively. We complete the description of the problem with appropriate far-field conditions

$$\mathbf{u} \to \mathbf{u}_\infty(\mathbf{x}, t), \quad p \to p_\infty(t), \quad \text{as } |\mathbf{x}| \to \infty, \tag{4}$$

where $\mathbf{u}_\infty$ is the velocity of the incident flow and p_∞ is in reference to a zero gas pressure inside one of the bubbles.

We now consider the motion of the interface. The kinematic condition states that material points on the interface move with the velocity of the fluid. Thus, the Lagrangian description is

$$\frac{d\mathbf{x}}{dt} = \mathbf{u}(\mathbf{x}), \quad \mathbf{x} \in \Gamma,$$

and many approaches to tracking interfaces are based on the time integration of the above (c.f. [29, 38, 41], for example). However, for longtime simulations where the interface changes shape significantly, the Lagrangian description may lead to either clustering of marker points or inadequate resolution of the interface. Instead, we employ the observation that the shape of the evolving interface is determined solely by the normal component of the fluid velocity, $U = \mathbf{u} \cdot \mathbf{n}$. Accordingly, a tangential component T can be added without changing the shape of the evolving curve, which can then be used to dynamically control the mesh. In [16], we investigated evolving

$$\frac{d\mathbf{x}}{dt} = U\mathbf{n} + T\mathbf{s}, \quad \mathbf{x} \in \Gamma, \tag{5}$$

where T is chosen to dynamically maintain an equal arclength spacing of marker points. This is called the *equal arclength frame*, and we saw in [16] that it eliminates the need to postprocess points and prevents prohibitively small time steps that can be required by explicit methods when points are allowed to cluster together.

The equal arclength frame is realized in the following manner. The interface Γ_k is parametrized by $\alpha \in [0, 2\pi]$ so that $\mathbf{x} = \mathbf{x}(\alpha, t)$ describes the interface. (To simplify notation, the parameter α is assumed to take on the appropriate values according to the particular Γ_k under consideration.) Let s be arclength, $0 \le s \le L_k$, where L_k is the total length of Γ_k. We require that $s_\alpha = |\mathbf{x}_\alpha|$ be everywhere equal to its mean,

$$s_\alpha = L_k/2\pi. \tag{6}$$

As derived in [14, 16], the appropriate choice for T is

$$T(\alpha, t) = T(0, t) - \int_0^\alpha \theta_{\alpha'} U \, d\alpha' + \frac{\alpha}{2\pi} \int_0^{2\pi} \theta_{\alpha'} U \, d\alpha', \tag{7}$$

where θ is the tangent angle to Γ. If the initial parametrization is such that (6) is satisfied, then choosing T according to (7) maintains this constraint in time.

3. THE BIHARMONIC EQUATION AND COMPLEX VARIABLE THEORY

For flow in two dimensions, the governing equations can be simplified by introducing a stream function $W(x, y)$, which satisfies the relations $u = W_y$, $v = -W_x$. The Stokes equations are replaced by the biharmonic equation for W,

$$\Delta^2 W(\mathbf{x}) = 0.$$

There is a powerful complex variable theory for the biharmonic equation that has been exploited by a number of authors (c.f. [1, 3, 13, 36] for example) to derive analytical solutions for a single interface in a creeping flow. This complex variable theory also provides the analytical tools for deriving the integral equations that are the basis for our numerical study. We summarize the relevant details of this theory here (c.f. [18] for derivations and more details).

Following the discussion of Mikhlin and others [23–25], we note that any plane biharmonic function $W(x, y)$ can be expressed by Goursat's formula as

$$W(x, y) = \mathrm{Re}(\bar{z}\phi(z) + \chi(z)),$$

where ϕ and χ are analytic functions of the complex variable $z = x + iy$, and $\mathrm{Re}(f)$ denotes the real part of the complex-valued function f. The functions $\phi(z)$ and $\psi(z) = \chi'(z)$ are known as Goursat functions. All of the relevant physical variables can be expressed in terms of these Goursat functions and they are listed here as

$$\begin{aligned} -v + iu &= \phi(z) + z\overline{\phi'(z)} + \overline{\psi(z)} \\ \zeta + ip &= -4\phi'(z), \end{aligned}$$

where $\zeta = -\nabla^2 W$ is the vorticity. These expressions allow us to reduce the boundary-value problems associated with interfaces in a Stokes flow to problems in analytic function theory, namely that of finding ϕ and ψ which satisfy appropriate conditions on the boundary Γ. We outline these conditions below.

For any point τ on a component boundary Γ_k, the outward normal is given by $n = -i\tau_s$. An expression for the stress acting on the interface is (c.f. [16, 17] for more details)

$$\Sigma\mathbf{n} \equiv -2\frac{\partial}{\partial s}(\phi - \tau\bar{\phi}' - \bar{\psi}). \tag{8}$$

Substituting the above and $\kappa n = -\tau_{ss}$ into the interface condition (2) or the viscous sintering problem and integrating with respect to s gives

$$\phi - \tau\bar{\phi}' - \bar{\psi} = -\frac{1}{2}\tau_s + a_k, \quad \tau \in \Gamma_k. \tag{9}$$

The constants of integration a_k may be fixed arbitrarily on one boundary, say $a_0 = 0$. However, in multiply-connected domains, they may differ on each contour and their values are obtained as part of the solution process (c.f. [10, 23, 24]). Similarly, the stress condition (3) for the bubble dynamics problem is equivalent to

$$\phi - \tau\bar{\phi}' - \bar{\psi} + \frac{i}{2}p_k\tau = -\frac{1}{2}\tau_s + i\frac{\mathcal{B}}{4}\int_0^s n_g\bar{\tau}\tau_s + \overline{n_g}\tau\tau_s\, ds + a_k, \quad \tau \in \Gamma_k. \tag{10}$$

Integrating (8) with respect to s about Γ_k gives the net force F_k, Specifically,

$$F_k = 2[\phi - \tau\bar{\phi}' - \bar{\psi}]_{\Gamma_k}, \tag{11}$$

where $[.]_{\Gamma_k}$ means the increment as the curve Γ_k is traversed in the clockwise direction. We see from the right-hand side of (9) that if the motion is driven by curvature alone, there can be no net force acting on Γ_k. However, if gravity is included, as is the case in (10), there is a contribution that becomes an important part of the integral equation formulation in Section 4.2. We isolate this value as

$$\begin{aligned} F_k &= -i\frac{\mathcal{B}}{2}\int_0^{L_k} n_g\bar{\tau}\tau_s + \overline{n_g}\tau\tau_s\, ds \\ &= -i\frac{\mathcal{B}}{2}\int_0^{L_k} n_g\left[\frac{1}{2}\frac{\partial}{\partial s}(x^2+y^2) + ixy_s - iyx_s\right] + \frac{\overline{n_g}}{2}\frac{\partial\tau^2}{\partial s}\, ds \\ &= -\mathcal{B}n_g\int_0^{L_k} yx_s\, ds \\ &= -\mathcal{B}n_g A_k, \end{aligned}$$

where A_k is the area bounded by Γ_k.

If D is unbounded or semi-infinite in extent, the Goursat functions must also capture the appropriate far-field behavior (4) (c.f. [36]),

$$\phi \sim -\frac{i}{4}p_\infty(t)z + \phi_\infty(z) + G(t), \quad \psi \sim \psi_\infty(z) - \overline{G(t)}, \quad \text{as } |z| \to \infty, \tag{12}$$

where $p_\infty(t)$ is determined as part of the solution, $G(t)$ is an arbitrary constant, and $\phi_\infty(z)$ and $\psi_\infty(z)$ are suitably chosen analytic functions so that

$$\phi_\infty(z) + z\overline{\phi'_\infty(z)} + \overline{\psi_\infty(z)} = -i(u_\infty + iv_\infty).$$

4. THE SHERMAN–LAURICELLA INTEGRAL EQUATION

We now consider the extension of the integral equation methods developed in [16] for a single, closed interface in a Stokes flow to multiply-connected domains. Unfortunately, a direct application of the integral equations for simply-connected problems will become rank deficient in multiply-connected domains. In [10], this rank deficiency was resolved for Stokes flow with solid boundaries and for isotropic elasticity in the plane. For example, in Stokes flow about particles with solid boundaries, fundamental singular solutions known as Stokeslets and Rotlets are added to each component curve. As discussed in that work, this process is akin to the completed double layer method used by many authors [19, 26–30] to construct nonsingular systems for second-kind integral equations. Here, we construct full-rank integral equations, however, the physical principles underlying viscous sintering and bubble dynamics require different resolutions. Thus, we consider these two cases separately.

4.1. Viscous Sintering: Bounded Domain

We consider the construction of functions ϕ and ψ that are used to satisfy the boundary condition (9). Recall that the sintering process acts to increase the cohesion of the domain D

with time and thus we expect the void spaces to decrease in area. We model this process by placing a source singularity in each component curve (this is the same approach discussed in [23, 38–40]). The strength of this singularity is related to the rate of change of area (see below). Motivated by the discussion in [16], the chosen representations for $\phi(z)$ and $\psi(z)$ are

$$\phi(z) = \frac{1}{2\pi i}\int_\Gamma \frac{\omega(\xi,t)}{\xi - z}\,d\xi,$$

$$\psi(z) = \frac{1}{2\pi i}\int_\Gamma \frac{-\overline{\omega(\xi,t)}\,d\xi + \omega(\xi,t)\,d\bar{\xi}}{\xi - z} - \frac{1}{2\pi i}\int_\Gamma \frac{\bar{\xi}\omega(\xi,t)}{(\xi - z)^2}\,d\xi + \sum_{k=1}^{M}\frac{b_k(t)}{z - z_k}.$$

Here, $\omega(\xi,t)$ is an unknown complex density, and z_k is an arbitrary fixed point inside the region bounded by Γ_k (z_k moves as the void space moves so as to remain inside Γ_k). The time-dependent singularity strengths $b_k(t)$ are strictly imaginary and are defined by

$$b_k = \int_{\Gamma_k} \omega(\tau,t)\,d\bar{\tau} - \overline{\omega(\tau,t)}\,d\tau, \quad k = 1\cdots M.$$

They give the rate of change of area inside the component curves Γ_k,

$$\frac{dA_k}{dt} = 2\pi i\overline{b_k}.$$

Substituting the representations into (9), letting z tend to a point τ on the contour Γ and using the classical formulae for the limiting values of Cauchy-type integrals, we obtain the Sherman–Lauricella integral equation,

$$\omega(\tau,t) + \frac{1}{2\pi i}\int_\Gamma \omega(\xi,t)\,d\ln\frac{\xi-\tau}{\bar{\xi}-\bar{\tau}} + \frac{1}{2\pi i}\int_\Gamma \overline{\omega(\xi,t)}\,d\frac{\xi-\tau}{\bar{\xi}-\bar{\tau}} - i\frac{\bar{B}_0}{\bar{\tau}-\bar{z}_*}$$
$$- \sum_{k=1}^{M}\frac{\overline{b_k(t)}}{\bar{\tau}-\bar{z}_k} - a_k(t) = -\frac{1}{2}\frac{\partial\tau}{\partial s}, \quad \tau\in\Gamma_k \tag{13}$$

where $a_0(t) = 0$, and for $k > 0$, we define

$$a_k = -\int_{\Gamma_k}\omega(\xi,t)\,ds.$$

Note that the left-hand side of the integral equation includes the term $\bar{B}_0/(\bar{\tau} - \bar{z}_*)$, where we let z_* be an arbitrary point in the fluid domain D and

$$B_0 = \frac{1}{2\pi}\int_\Gamma\left[\frac{\omega(\tau,t)}{(\tau - z_*)^2}\,d\tau - \frac{\overline{\omega(\tau,t)}}{(\bar{\tau}-\bar{z}_*)^2}\,d\bar{\tau}\right].$$

The integral equation (13) has been well studied in the context of elasticity in the plane, we refer the readers [24, 25] for a proof of invertibility and that $B_0 = 0$ if the boundary data satisfy the compatibility condition

$$\mathrm{Im}\int_\Gamma \overline{\frac{\partial\tau}{\partial s}}\,d\tau = 0,$$

which is clearly the case. We will simply observe here that the equation is a Fredholm equation of the second kind and, in the absence of the source terms, the integral equation above is singular with rank deficiency M.

4.2. Bubble Dynamics: Unbounded and Semi-infinite Domains

We consider now the case in which Γ_k are the boundaries of gas bubbles, moving and deforming under the action of hydrodynamic and applied forces. There are three elements distinct from the previous example of viscous sintering that impact the representations of the Goursat functions. First, ϕ and ψ must capture the far-field behavior given by (12). Second, the bubbles must conserve mass and thus cannot contain source terms. Finally, when gravity effects are included, the Goursat functions must be multivalued according to (11). We must also resolve the additional complication of Stokes paradox: if there is a net force acting on the assemblage of bubbles, then the velocity at infinity grows logarithmically. As a result, when gravity effects are included, we can only consider these flows in semi-infinite domains. The necessary modifications are discussed at the end of this section.

Appropriate representations for the Goursat functions are

$$\phi(z) = \frac{1}{2\pi i}\int_\Gamma \frac{\omega(\xi,t)}{\xi - z}\,d\xi - \frac{i}{4}p_\infty(t)z + \phi_\infty(z) + G(t) + \sum_{k=1}^{M} C_k \log(z - z_k),$$

$$\psi(z) = \frac{1}{2\pi i}\int_\Gamma \frac{-\overline{\omega(\xi,t)}\,d\xi + \omega(\xi,t)\,d\bar{\xi}}{\xi - z} - \frac{1}{2\pi i}\int_\Gamma \frac{\bar{\xi}\omega(\xi,t)}{(\xi - z)^2}\,d\xi + \psi_\infty(z) - \overline{G(t)}$$
$$+ \sum_{k=1}^{M}\left\{\overline{C_k}\log(z - z_k) - C_k\frac{\bar{z}_k}{z - z_k}\right\}.$$

In the above, Stokeslet singularities of strength C_k are added to each component curve. As discussed in detail in [17], their strength is related to the force acting on each bubble through $F_k = -8\pi i C_k$, thus

$$C_k = -i\frac{\mathcal{B}n_g A_k}{8\pi}. \tag{14}$$

Again, substituting the above forms into (10) and letting z approach a boundary point τ, we obtain

$$\omega(\tau,t) + \frac{1}{2\pi i}\int_\Gamma \omega(\xi,t)\,d\ln\frac{\xi - \tau}{\bar{\xi} - \bar{\tau}} + \frac{1}{2\pi i}\int_\Gamma \bar{\omega}(\xi,t)\,d\frac{\xi - \tau}{\bar{\xi} - \bar{\tau}} - \frac{i}{2}(p_\infty - p_k)\tau - \tilde{a}_k$$
$$= -\frac{1}{2}\frac{\partial\tau}{\partial s} - \phi_\infty(\tau) + \tau\overline{\phi'_\infty(\tau)} + \overline{\psi_\infty(\tau)} + i\frac{\mathcal{B}}{4}\int_0^\alpha n_g\bar{\tau}\tau_{\alpha'} + \overline{n_g}\tau\tau_{\alpha'}\,d\alpha'$$
$$- \sum_{k=1}^{M}\left\{2iC_k\arg(\tau - z_k) - \overline{C_k}\frac{\tau - z_k}{\bar{\tau} - \overline{z_k}}\right\}, \tag{15}$$

where $\tilde{a}_k(t) \equiv a_k(t) - 2G(t)$ are given by

$$\tilde{a}_k = -\int_{\Gamma_k}\omega(\xi,t)\,ds.$$

We must also define representations for the pressure terms that will result in well-conditioned integral equations. Following [16], the far-field pressure is defined by

$$p_\infty(t) = -\frac{2}{\pi}\mathrm{Re}\int_{\Gamma_1}\frac{\omega(\xi,t)}{(\xi - z_1)^2}\,d\xi,$$

and the gas pressure in each bubble is

$$p_k(t) = p_\infty(t) + \frac{2}{\pi}\mathrm{Re}\int_{\Gamma_k}\frac{\omega(\xi,t)}{(\xi - z_k)^2}\,d\xi.$$

This gives a reference value of zero gas pressure inside Γ_1.

Semi-Infinite Domains. In an unbounded domain, the leading term of the velocity in the far field derived from the previous representations of the Goursat functions is

$$-v + iu \sim 2\left(\sum_{m=1}^{M} C_m\right)\log|z|, \quad \text{as } |z| \to \infty.$$

Thus, if gravity effects are included and the values of C_k are given by (14), the velocity grows logarithmically. This is a consequence of Stokes paradox, and we can eliminate this difficulty by introducing an infinite wall into the fluid domain and assuming that the bubbles are embedded in a half space S. (Alternatively, we could allow logarithmic behavior and match our solution to an outer Oseen solution; c.f. [37]. We do not consider this case here.) By convention, we assume that S is the the upper half plane so that the wall boundary Γ_W is given by $y = 0$, and on that wall boundary, the fluid velocity is zero. (Manga and Stone implemented a similar fix in [21] by introducing a planar free-slip surface.) By changing the direction of gravity, $\mathbf{n_g}$ in (3), it is trivial to change the relative position of the solid wall. The boundary condition on the wall is satisfied by using the method of images, and formulae for the reflected sources are given in [17]. The reflected Stokeslets act to cancel out the logarithmic growth of the velocity field, and we can then match to the appropriate far-field velocity as given by (12).

4.3. Dynamics of the Interface

As discussed in Section 2, the shape of the evolving interface is determined solely by the normal component of the fluid velocity U on Γ, where $U = \mathrm{Re}\{(u + iv)\bar{n}\}$ and

$$\begin{aligned} u + iv &= -i\lim_{z\to\tau}(\phi + z\bar{\phi}' + \bar{\psi}), \quad \tau \in \Gamma \\ &= -\frac{1}{2\pi}\oint_\Gamma \omega(\xi,t)\left\{\frac{d\xi}{\xi - \tau} + \frac{d\bar{\xi}}{\bar{\xi} - \bar{\tau}}\right\} + \frac{1}{2\pi}\int_\Gamma \overline{\omega(\xi,t)}d\left(\frac{\xi - \tau}{\bar{\xi} - \bar{\tau}}\right) \\ &\quad + u_\infty + iv_\infty + (u + iv)^s. \end{aligned} \tag{16}$$

In the above, $\omega(\tau, t)$ is found from the solution to (13) or (15) and $\oint$ denotes a principal value integral. It is understood that $u_\infty + iv_\infty \equiv 0$ for flows in bounded domains and $(u + iv)^s$ takes on the value from the appropriate singular contributions: sources in the case of viscous sintering and Stokeslets in the case of bubble dynamics. The work in [16] presents a thorough analysis of the evolution equation for a single interface in a creeping flow. Specifically, we

performed a small-scale decomposition of (5) to determine the most dominant term (the leading-order term at small spatial scales). In the equal arclength frame this term is

$$\frac{d\tau}{dt} \sim -\frac{1}{4}\frac{\mathcal{H}[\tau_\alpha]}{s_\alpha(t)}, \quad \tau \in \Gamma_k,$$

where $\mathcal{H}[.]$ is the Hilbert transform. For explicit time stepping methods, this leads to a low-order CFL-type stability constraint.

5. NUMERICAL METHODS

5.1. Spectral Description of the Interface and Time Integration Schemes

We obtain an initial equal arclength distribution of marker points on each Γ_k by the methods described in [14]. Briefly outlining this procedure, we start with an even number of points, N_k on Γ_k, given in some convenient parametrization. We assume that N_k is large enough to fully resolve the interface (i.e., the Fourier spectrum has decayed to round-off). The initialization procedure involves solves a sequence of nonlinear equations for the N_k marker points at equal arclength intervals using Newton's method and Fourier interpolation. Once this is done, Γ_k is represented by a spectral mesh with node points at uniformly spaced intervals in α ($h_k = 2\pi/N_k$ is the mesh spacing).

As discussed briefly in the previous section and in more detail in [16], the stability constraint on an explicit method is

$$\Delta t = O\left(\min_{\Gamma_k} \frac{L_k}{N_k}\right). \tag{17}$$

Even when regions of high curvature develop, the evolution of the interface is not stiff as long as grid points are maintained at equispaced intervals. Based on our analysis in [16], we choose the explicit midpoint Runge–Kutta method for the time integration of (5).

The right-hand side of the evolution equation (5) is calculated pseudospectrally: all differentiation in α is done using the fast Fourier transform and the fluid velocity is obtained through a spectrally accurate discretization (see Section 5.2). As discussed in detail in [16], we see growth of modes near the Nyquist frequency, particularly if the initial profile is significantly deformed. In [16], we carefully considered stability issues that might have been masked by filtering, and thus we removed this instability by padding the Fourier spectrum. Based on our understanding developed from this previous work, we are confident that using the less expensive procedure of filtering will not smooth out any important effects. We use the filter from [14] which combines a 25th-order Fourier filter

$$\hat{\Pi}[f](k) = e^{-10(|k|/N)^{25}} \hat{f}(k)$$

with a Krasny filter, setting to zero all Fourier modes below a tolerance level $\epsilon = 10^{-13}$.

The Fourier spectrum is checked during the course of simulation and if the modes near the Nyquist frequency rise above round off, N_k is doubled. Similary, if the modes at the tail of the spectrum have decayed sufficiently, N_k is cut in half. The time step is adjusted according to the stability constraint (17).

5.2. Discretization of Integral Equation

In order to solve the Sherman–Lauricella equations, we use a Nyström discretization based on the trapezoidal rule since it achieves super-algebraic convergence for smooth data on smooth boundaries. For this, we let the position of each nodal point on Γ_k be described by τ_j^k. Associated with each such point is an unknown value ω_j^k. The derivative $\partial\tau^k/\partial\alpha$ is denoted by σ^k and the derivative values σ_j^k at the discretization points are obtained pseudospectrally. The total number of points is

$$N = \sum_{k=k_0}^{M} N_k,$$

where $k_0 = 0$ for problems in bounded domains and $k_0 = 1$ for problems in unbounded or semi-infinite domains.

Before considering the discretization of (13) and (15), we define the discrete kernels of the integral operators:

$$K_1\left(\tau_j^k, \tau_n^m\right) = \frac{h_m}{2\pi i}\left(\frac{\sigma_n^m}{\tau_n^m - \tau_j^k} - \frac{\overline{\sigma_n^m}}{\overline{\tau_n^m - \tau_j^k}},\right)$$

$$K_2\left(\tau_j^k, \tau_n^m\right) = \frac{h_m}{2\pi i}\left(\frac{\sigma_n^m}{\overline{\tau_n^m - \tau_j^k}} - \frac{\overline{\sigma_n^m}\left(\tau_n^m - \tau_j^k\right)}{\left(\overline{\tau_n^m - \tau_j^k}\right)^2}\right).$$

When $\tau_j^k = \tau_n^m$, K_1 and K_2 should be replaced by the appropriate limits [10, 16]

$$K_1\left(\tau_j^k, \tau_j^k\right) = \frac{h_k}{2\pi}\kappa_j^k\left|\sigma_j^k\right|,$$

$$K_2\left(\tau_j^k, \tau_j^k\right) = \frac{h_k}{2\pi}\kappa_j^k\frac{\left(\sigma_j^k\right)^2}{\left|\sigma_j^k\right|},$$

where κ_j^k denotes the curvature at the point τ_j^k and is calculated pseudospectrally.

Consider now the system (13). After discretization, we have

$$\omega_j^k + \sum_{m=0}^{M}\sum_{n=1}^{N_m} K_1^v\left(\tau_j^k, \tau_n^m\right)\omega_n^m + \sum_{m=0}^{M}\sum_{n=1}^{N_m} K_2^v\left(\tau_j^k, \tau_n^m\right)\overline{\omega_n^m} = -\frac{1}{2}\frac{\sigma_j^k}{\left|\sigma_j^k\right|}, \tag{18}$$

where

$$K_1^v\left(\tau_j^k, \tau_n^m\right) = K_1\left(\tau_j^k, \tau_n^m\right) + h_m\left|\sigma_n^m\right|\delta_{km} + \frac{h_m\overline{\sigma_n^m}}{\overline{\tau_n^m} - \overline{z_m}}\delta_{mm}$$

$$K_2^v\left(\tau_j^k, \tau_n^m\right) = K_2\left(\tau_j^k, \tau_n^m\right) - \frac{h_m\sigma_n^m}{\overline{\tau_n^m} - \overline{z_m}}\delta_{mm}.$$

In the preceding expressions, δ_{km} is the usual Kronecker delta symbol, except that $\delta_{00} \equiv 0$.

Remark. We have omitted the term B_0 in Eq. (13) since its absence does not affect the behavior of the iterative solution procedure we will employ. For a detailed discussion of this point, see [7].

Consider now the system (15). After discretization, we have

$$\omega_j^k + \sum_{m=1}^{M}\sum_{n=1}^{N_m} K_1^b\left(\tau_j^k, \tau_n^m\right)\omega_n^m + \sum_{m=1}^{M}\sum_{n=1}^{N_m} K_2^b\left(\tau_j^k, \tau_n^m\right)\overline{\omega_n^m} = f_j^k, \tag{19}$$

where

$$\begin{aligned} f_j^k = & -\frac{1}{2}\frac{\sigma_j^k}{\left|\sigma_j^k\right|} - \phi_\infty\left(\tau_j^k\right) + \tau_j^k\overline{\phi_\infty'\left(\tau_j^k\right)} + \overline{\psi_\infty\left(\tau_j^k\right)} + \frac{i\mathcal{B}}{4}\int_0^{jh_k} n_g\,\bar{\tau}\,\tau_{\alpha'} + \overline{n_g}\,\tau\,\tau_{\alpha'}\,d\alpha' \\ & - \sum_{m=1}^{M}\left\{2iC_m \arg\left(\tau_j^k - z_m\right) - \overline{C_m}\frac{\tau_j^k - z_m}{\overline{\tau_j^k} - \overline{z_m}}\right\}. \end{aligned}$$

The kernels K_1^b and K_2^b are given by

$$\begin{aligned} K_1^b\left(\tau_j^k, \tau_n^m\right) &= K_1\left(\tau_j^k, \tau_n^m\right) + h_m\left|\sigma_n^m\right|\delta_{km} + \frac{i}{2\pi}\frac{h_m\sigma_n^m}{\left(\tau_n^m - z_m\right)^2}\delta_{km}\tau_j^k \\ K_2^b\left(\tau_j^k, \tau_n^m\right) &= K_2\left(\tau_j^k, \tau_n^m\right) + \frac{i}{2\pi}\frac{h_m\overline{\sigma_n^m}}{\left(\overline{\tau_n^m} - \overline{z_m}\right)^2}\delta_{km}\tau_j^k. \end{aligned}$$

In our implementation, the matrix equations (18) and (19) are solved iteratively, using the generalized minimum residual method GMRES [34]. As discussed in detail in [10, 16, 17], the bulk of the work at each iteration lies in applying the full matrix to a vector, i.e., computing the product represented by the left-hand side of (18) and (19). This product can be computed in $O(N)$ time using the adaptive fast multipole method (FMM). The implementation used here was developed in [10] for problems in Stokes flow with solid boundaries and elasticity in the plane. For further details, we also refer the reader to the original papers [4, 8, 33]. Since the number of iterations needed to solve a Fredholm equation of the second kind to a fixed precision is bounded independent of the system size, we can estimate the total cost of solving the stress problem by

$$c(\epsilon)\,C(\epsilon)\,N,$$

where $c(\epsilon)$ is the number of GMRES iterations needed to reduce the residual error to ϵ and $C(\epsilon)$ is the constant of proportionality in the FMM.

Once the solution ω_j^k has been computed, we discretize (16) and calculate the velocity at the grid points according to

$$\begin{aligned} u_j^k + iv_j^k = & -\frac{h_k}{\pi}(\omega_\alpha)_j^k + \sum_{m=k_0}^{M}\sum_{n=1}^{N_m} K_1'\left(\tau_j^k, \tau_n^m\right)\omega_n^m + i\sum_{m=k_0}^{M}\sum_{n=1}^{N_m} K_2\left(\tau_j^k, \tau_n^m\right)\overline{\omega_n^m} \\ & + (u_\infty + iv_\infty)_j^k + \left(u_j^k + iv_j^k\right)^s, \end{aligned} \tag{20}$$

where $(u_\infty + iv_\infty)_j^k$ is taken to be zero in the case $k_0 = 0$; $(u_j^k + iv_j^k)^s$ takes on the appropriate values according to the contributions from the singularities in Γ_k; and K_2 is defined

previously and K_1' is

$$K_1'(\tau_j^k, \tau_n^m) = -\frac{h_m}{2\pi}\left(\frac{\sigma_n^m}{\tau_n^m - \tau_j^k} + \frac{\overline{\sigma_n^m}}{\overline{\tau_n^m - \tau_j^k}}\right)$$
$$K_1'(\tau_j^k, \tau_j^k) = -\frac{h_k}{2\pi}\mathrm{Re}\left\{\frac{(\sigma_\alpha)_j^k}{\sigma_j^k}\right\}.$$

The quadrature rule in (20) is spectrally accurate and is based on subtracting off the singularity in the principal value integral in (16). Again, FMM is used to evaluate (20). We note that in the primitive variable formulation, the integral equation is formulated in terms of the velocity, and thus an extra evaluation is not required after the integral equation has been solved. The cost of the extra calculation in (20) in our formulation is equivalent to one extra GMRES iteration and thus is not significant.

6. NUMERICAL RESULTS

The algorithms described above have been implemented in Fortran. Here, we illustrate their performance on a variety of examples. The convergence tolerance for the GMRES iteration is set to 10^{-10} and all timings cited are for a Compaq Alpha ES40. As a general check of the correctness of our integral equation methods, we calculated the velocities on the interface according to (20) for several examples and used these as input for our integral equation solvers developed in [10]. We confirmed that the solutions returned from these solvers satisfied the boundary conditions given by (9) and (10).

EXAMPLE 1. The sintering of a circular disk with a circular hole. To test our numerical methods, we first consider the evolution of a circular region filled with a viscous fluid and containing a circular hole centered at the origin. An analytical solution for this problem is given in [39], describing the shrinkage rate of the outer boundary and the inner hole. If r_o is the radius of the outer boundary, with $r_o(0) = R_o$, and r_i the radius of the inner, with $r_i(0) = R_i$, then the solution is described implicitly by

$$\begin{aligned} t &= 2(R_i - r_i) + \sqrt{3 + 4r_i^2} - \sqrt{3 + 4R_i^2}, \\ t &= 2(r_o - R_o) - \sqrt{4r_o^2 - 3} + \sqrt{4R_o^2 - 3}. \end{aligned} \tag{21}$$

The sintering process is shown in Fig. 2 for an example with an initial outer radius of $R_o = 1$ and inner radius of $R_i = 1/2$. Figure 3 shows the computed decay of the inner and outer radius and a comparison to the analytical solution (21).

In the next example, the interior circle is offset so that it is situated near the outer boundary. This example was considered in [30, 39] and it provides a useful comparison of our numerical methods against low-order accurate schemes. (The methods in [39] use a polygonal approximation to the interface and are constrained by the $O(N^3)$ operation count. Thus, they tend to be under resolved.) For the circular hole, we take a radius of 0.5 and situate the center at $y = 0.45$ on the vertical axis, giving an initial separation of 0.05 from the outer boundary. The initial time step is $\Delta t = 0.005$ and the boundaries are discretized with 512 points on each to ensure the solution is spectrally resolved during the first time step. This number is adjusted during the course of the simulation to ensure full resolution.

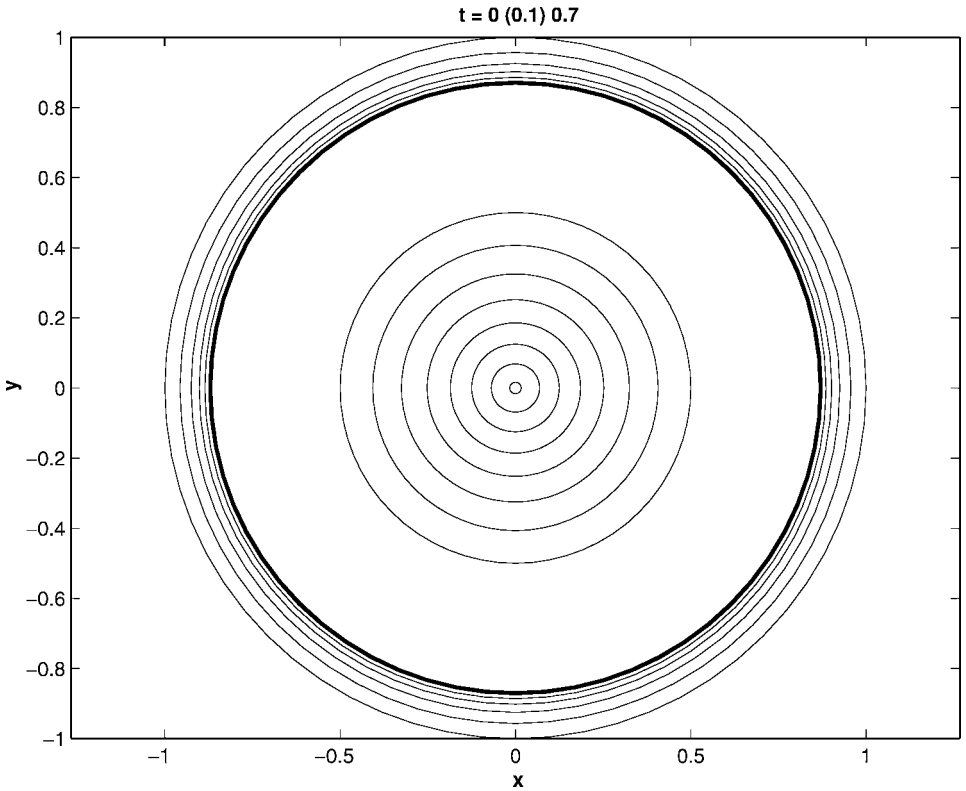

FIG. 2. The sintering of a circular disk with a circular hole at $t = 0(0.1)0.7$.

The total CPU time is 760 seconds and the initial and subsequent geometries are shown in Fig. 4. A comparison with the numerical results of van de Vorst are shown in Fig. 5, and the discrepancy between the two is significant. At $t = 0.1$, for example, the relative difference is about 10%. The error in total area of the fluid domain reported in their simulation has a

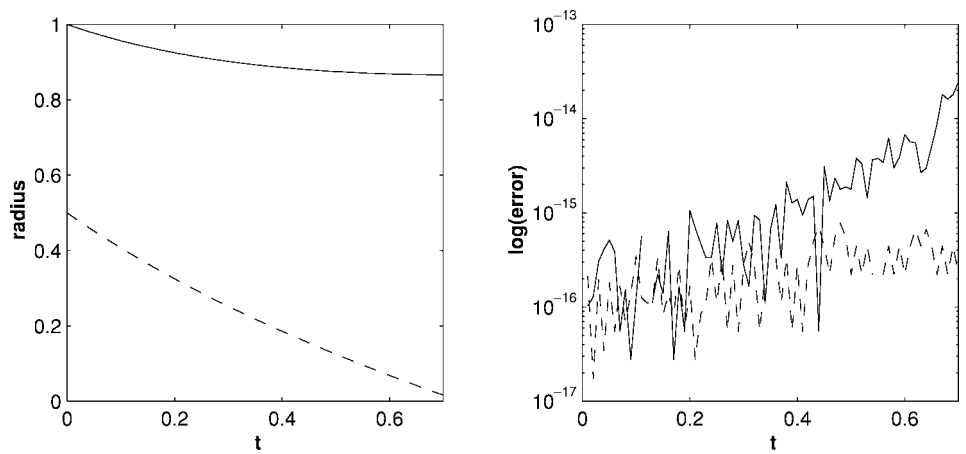

FIG. 3. The left-hand plot shows the behavior of the inner (dashed line) and outer (solid line) radius. The right-hand plot shows the error in the computed solution with $\Delta t = 0.01$ and $N = 64$ on each boundary.

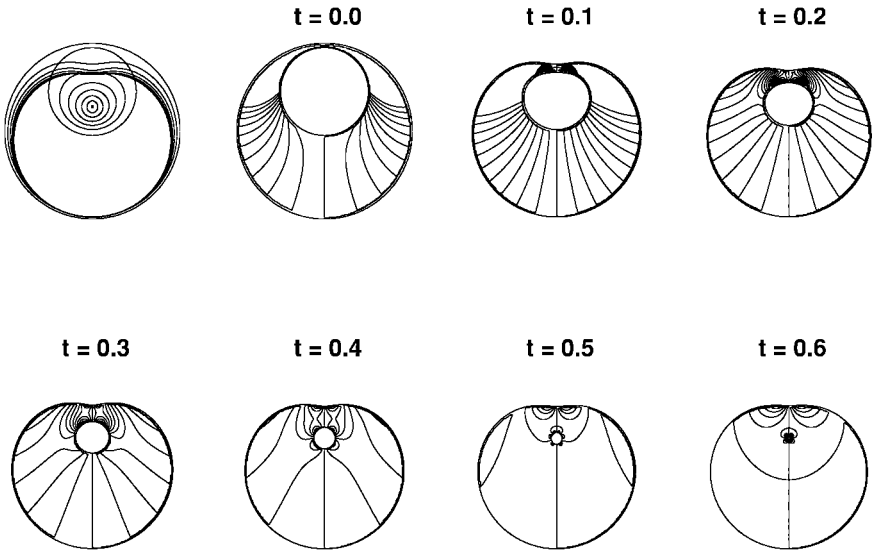

FIG. 4. The shrinkage of a circular hole located close to the outer boundary. The first plot shows the evolving geometry and the remaining plots show contours of vorticity at various times (equal contour levels are on all plots—hence the void regions shown at $t = 0.0$ and 0.1).

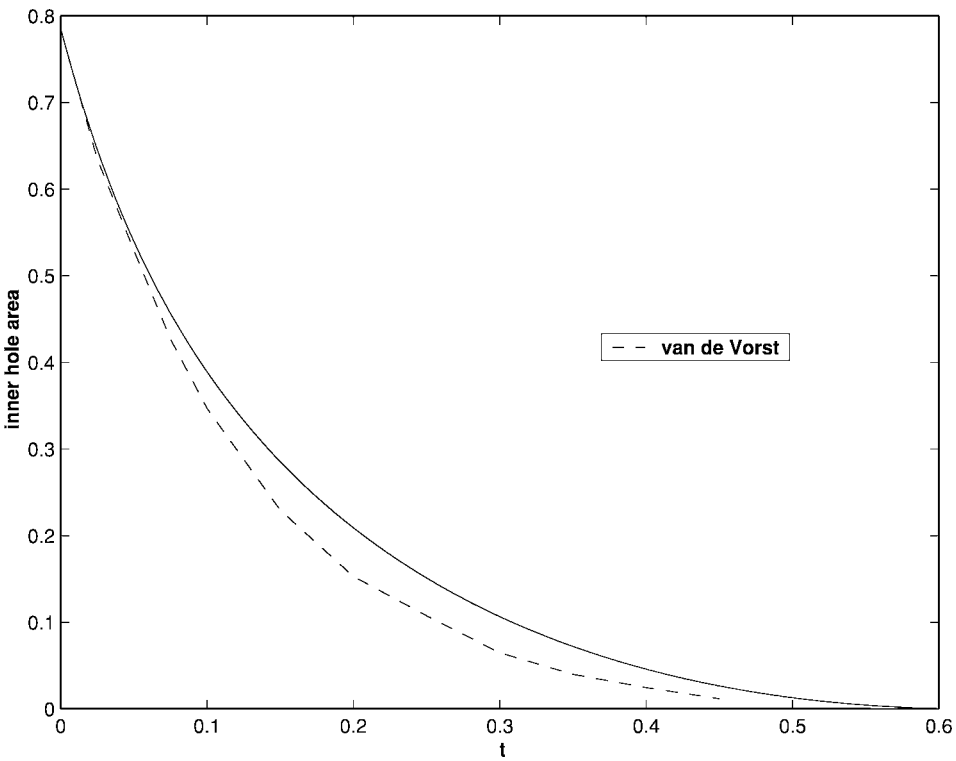

FIG. 5. A comparison of the computed decay of the area of a hole located close to the outer boundary versus the numerical results of van de Vorst [39].

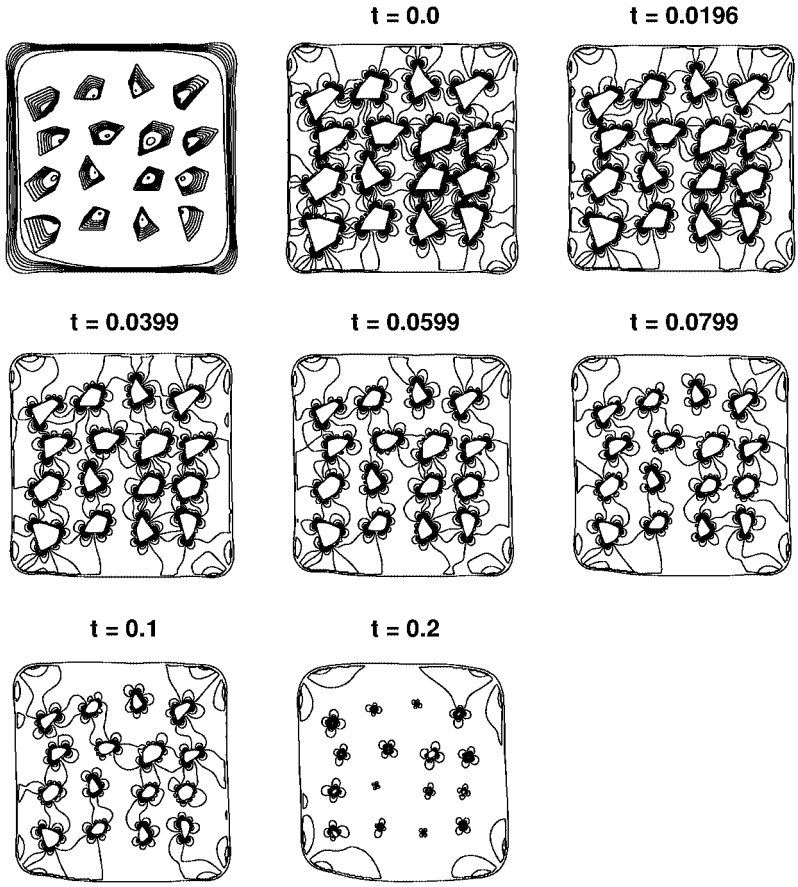

FIG. 6. The shrinkage of a rectangular region with 16 holes.

maximum value of 1%. In contrast, the error in area during our simulations remains below 0.0001%. The numerical methods presented in [30] are of higher order than those of [39], and their results on this test problem are in higher visual agreement with ours.

In this last sintering example, we consider the more complex problem shown in Fig. 6. The initial geometry is descretized with a total of 13,600 points (800 per hole). This number increases during the simulation to a maximum of 53,600 and then drops to a final value of 5400 at $t = 0.2$. The total CPU for this example is 45 hours.

EXAMPLE 2. Buoyancy-driven interactions between bubbles. In this next example, we consider the buoyancy-driven interaction between the 102 bubbles shown in Fig. 7, for three different values of the bond number $\mathcal{B} = 0.1$, 1.0, and 10.0. The bubbles are initially discretized with $N_k = 64$, and this number increases as the bubble deforms. The simulations for the three different values of Bond number are shown in Figs. 8–10. (Note that for comparison purposes, the reported time has been scaled by the Bond number, $t/\mathcal{B}$.) We can see in these simulations that the bubbles tend to move from regions of low concentration to regions of high concentration. This phenonemon was discussed in detail in [22]. A comparison of the three simulations at the final time is shown in Fig. 11. This final shows the greater deformation of bubbles with higher values of the Bond number. It also shows the increased mobility as a result of greater bubble deformations.

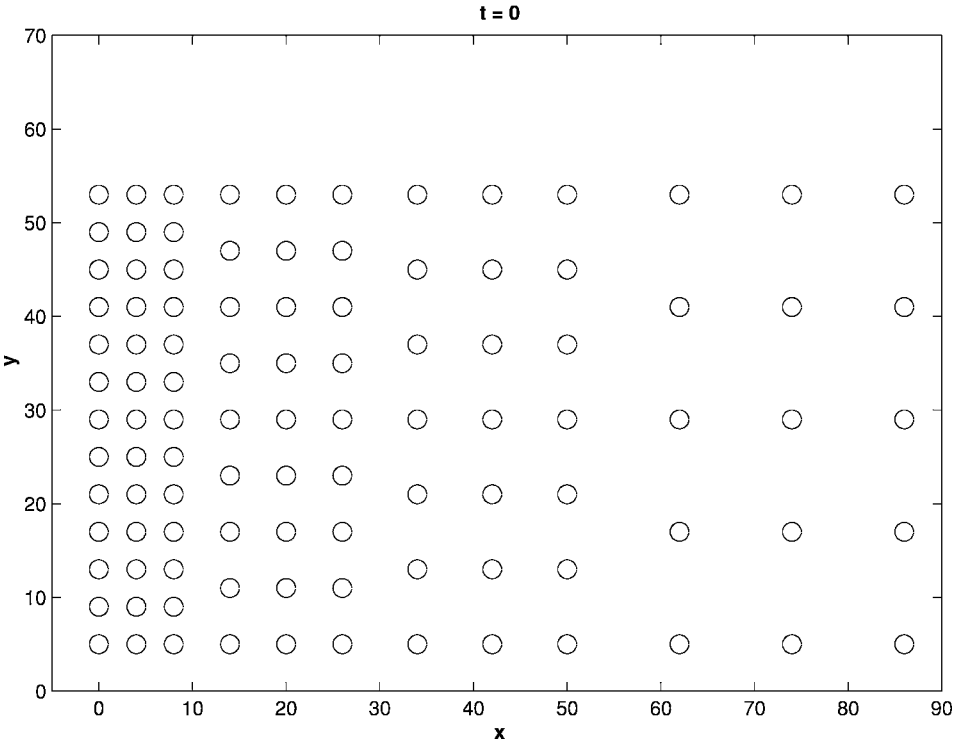

FIG. 7. The initial configuration of 102 air bubbles.

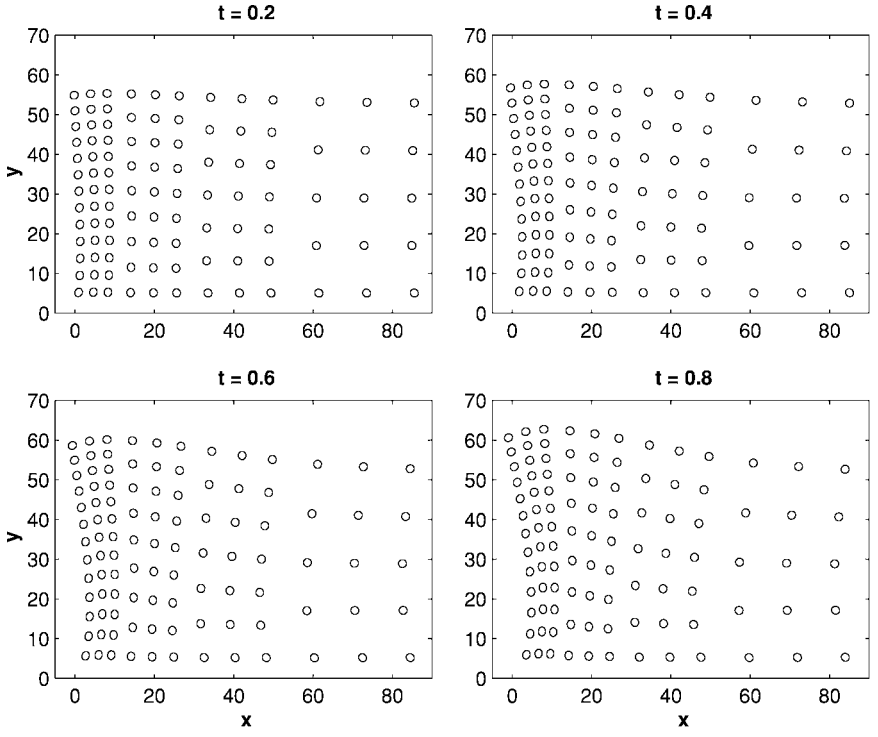

FIG. 8. Deformation with $\mathcal{B} = 0.1$, in presence of a wall at $y = 0$. The CPU time required for this simulation was 1.2 hours, error (A) $= 1.5035 \times 10^{-7}$, error $(s_\alpha) = 2.9003 \times 10^{-6}$. $\Delta t^0 = 0.01$, $\Delta t^f = 5.0237 \times 10^{-2}$, max $N_k =$ 128 and $N^f = 7616$.

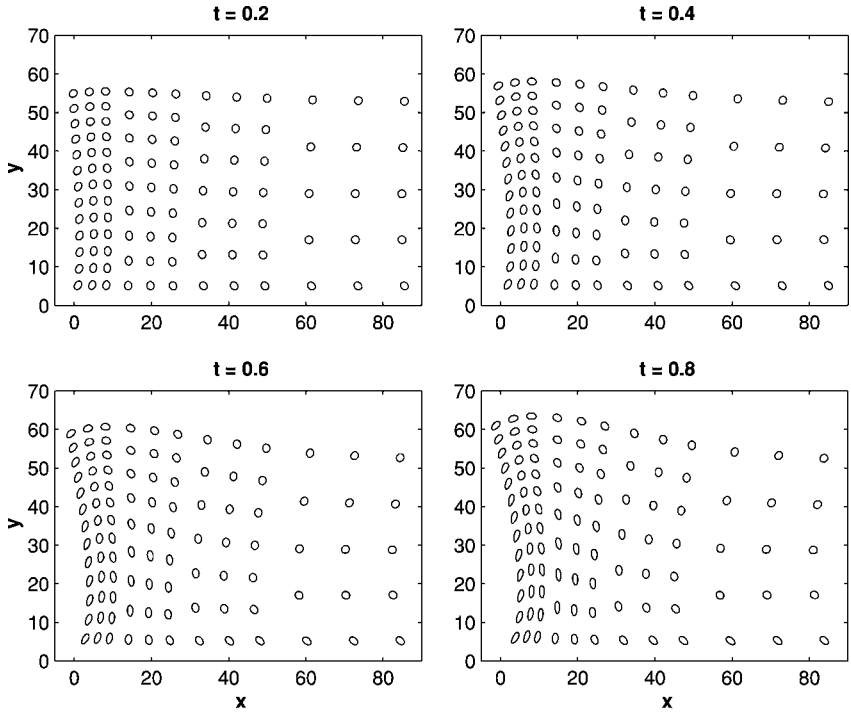

FIG. 9. Deformation with $\mathcal{B} = 1.0$, in presence of a wall at $y = 0$. The CPU time required for this simulation was 8.1 hours, error (A) $= 2.4617 \times 10^{-9}$, error $(s_\alpha) = 4.0836 \times 10^{-7}$. $\Delta t^0 = 0.01$, $\Delta t^f = 7.2647 \times 10^{-4}$ max $N_k = 1024$ and $N^f = 28352$.

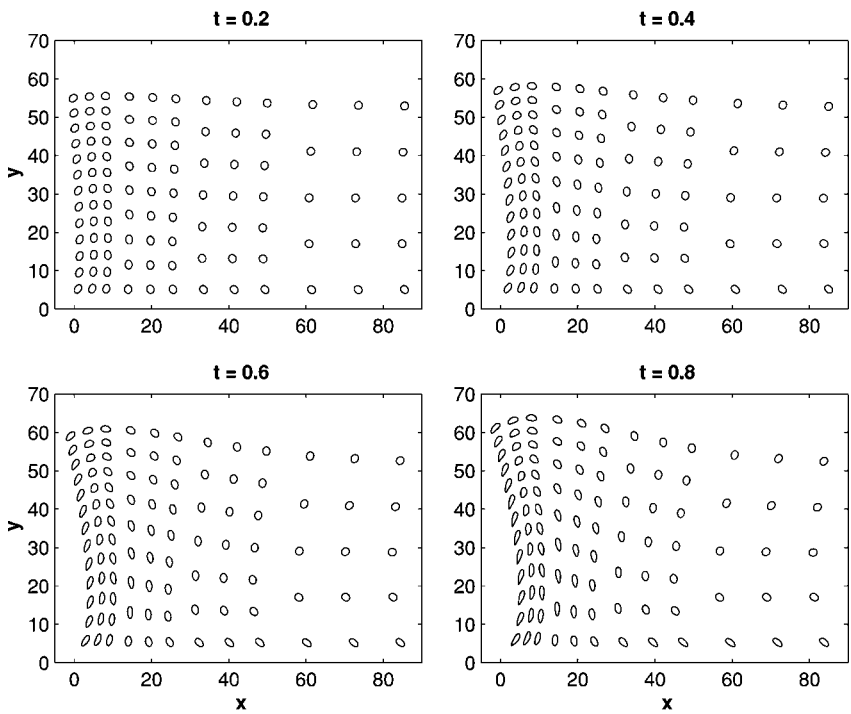

FIG. 10. Deformation with $\mathcal{B} = 10.0$, in presence of a wall at $y = 0$. The CPU time required for this simulation was 5 days, error (A) $= 4.1311 \times 10^{-10}$, error $(s_\alpha) = 6.2238 \times 10^{-7}$. $\Delta t^0 = 0.01$, max $N_k = 4096$, $N^f = 70272$.

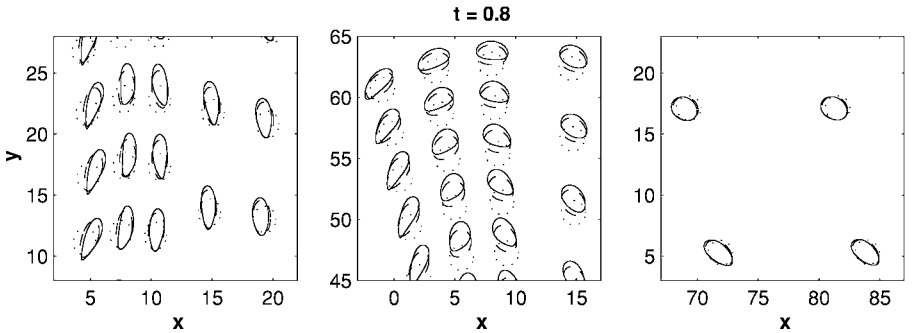

FIG. 11. A close up of three simulations at final time. The bubbles given by the solid contours have $\mathcal{B} = 10$, the dashed contours have $\mathcal{B} = 1$, and the dotted contours have $\mathcal{B} = 0.1$.

EXAMPLE 3. Polydispersed suspension of bubbles in an extensional flow. In this final example, we consider the deformation of a large number of bubbles (181) in an extensional flow,

$$u_\infty = \mathcal{C}x, \quad v_\infty = -\mathcal{C}y.$$

$\mathcal{C}$ is the dimensionless capillary number defined by

$$\mathcal{C} = \frac{\gamma \mu a}{\sigma},$$

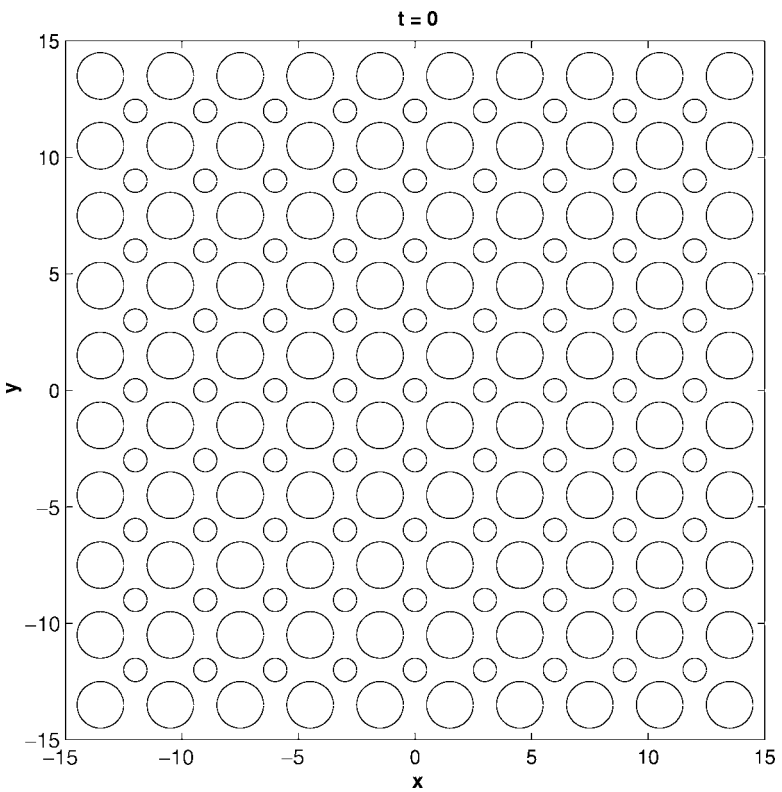

FIG. 12. Initial distribution of 181 bubbles in an extensional flow. The initial discretization places 128 points on the large bubbles, 64 on the small.

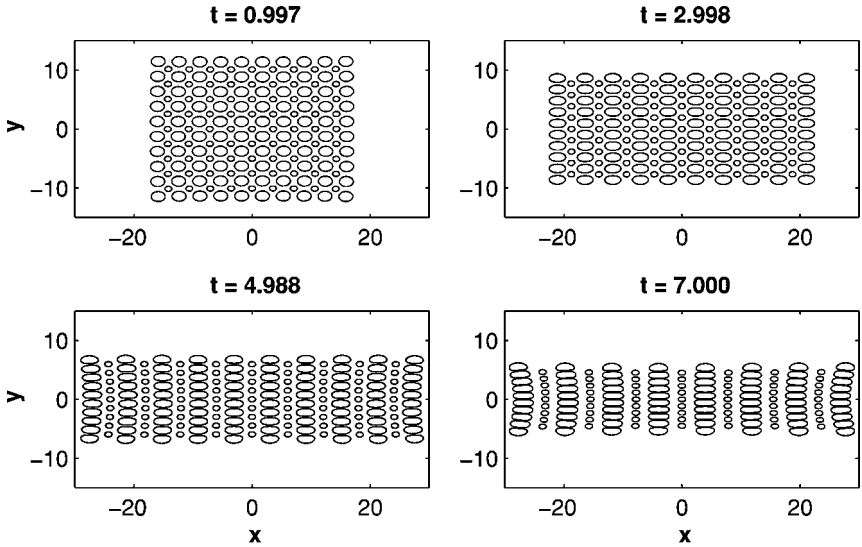

FIG. 13. Deformation of bubbles in an extensional flow with $\mathcal{C} = 0.15$. The CPU time required for this simulation was 3 days, 10 hours, error (A) $= 2.1479 \times 10^{-7}$, error $(s_\alpha) = 4.6387 \times 10^{-6}$. $\Delta t^0 = 0.025$, $\Delta t^f = 0.00297$, $\max N_k = 512$, $N^f = 40064$.

where γ is the characteristic strain rate of the extensional flow. The initial distribution of bubbles is shown in Fig. 12 and snapshots of the evolution are shown in Fig. 13. The total CPU time for this simulation was 3 days and 10 hours, with the great majority of time being spent computing the solution between $t = 5$ and the final time, $t = 7$ (63.2 hours). As the bubbles get closer together (see Fig. 14), the number of iterations required to solve

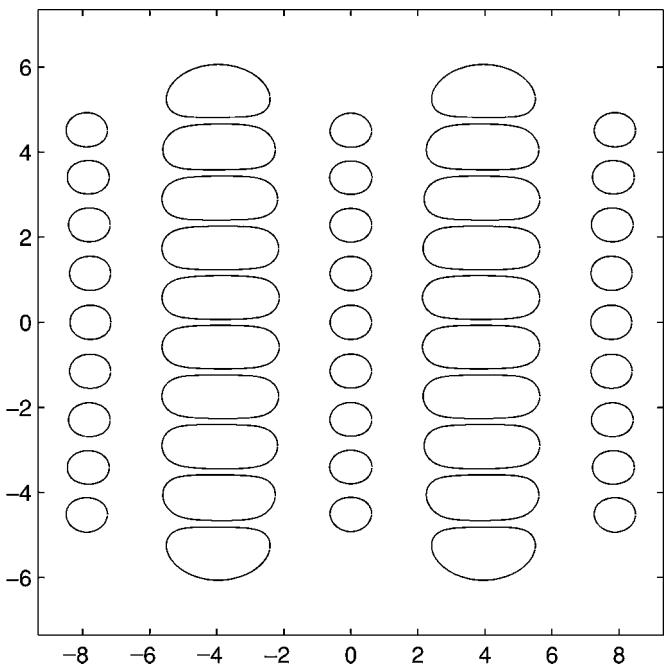

FIG. 14. A close up at $t = 7.0$.

matrix equations goes up significantly (from 24 iterations initially to at least 100 near the final time). It is expected that this expense can be alleviated by employing preconditioners and/or alternative quadratures. This will be investigated further.

7. CONCLUSIONS

In this paper, we extend the integral equation methods developed in [16] for a single, closed interface to those that are capable of handling multiple interfaces. These methods are efficient and highly accurate and should be attractive for studying large-scale problems in which a high degree of precision is needed to capture the precise nature of bubble interactions. We demonstrate the accuracy and efficiency of our methods using several examples, many involving $O(100)$ interfaces. In the future, these integral equation methods could be embedded in a periodic solver of the kind discussed in [9], in order to accurately study the rheological properties of suspensions and emulsions, for example.

Our methods incorporate several new ideas. The first involves "completing" the rank-deficiency of the integral operator in multiply-connected domains in the context of the complex-variable formulation. This was discussed for two separate cases: bubble dynamics and viscous sintering. In addition, the interfaces are described using a spectral mesh, and the velocity at the marker points is calculated pseudo-spectrally from the solution to the integral equations. The solution to the integral equation relies on a fast multipole-based iterative procedure which requires only $O(N)$ operations, where N is the total number of marker points. A final key feature in our methods is that evolution equations that preserve equal arclength spacing of the marker points are used, which results in a low-order stability constraint.

REFERENCES

1. L. K. Antanovskii, A plane inviscid incompressible bubble placed within a creeping viscous flow: Formation of a cusped bubble, *Eur. J. Mech. B/Fluids* **13**, 491 (1994).
2. U. M. Ascher and L. R. Petzold, *Computer Methods for Ordinary Differential Equations and Differential Algebraic Equations* (Soc. for Industr. & Appl. Math., Philadelphia, 1998).
3. J. D. Buckmaster and J. E. Flaherty, The bursting of two-dimensional drops in slow viscous flow, *J. Fluid Mech.* **60**, 625 (1973).
4. J. Carrier, L. Greengard, and V. Rokhlin, A fast adaptive multipole algorithm for particle simulations, *SIAM J. Sci. Statist. Comput.* **9**, 669 (1988).
5. R. Charles and C. Pozrikidis, Significance of the dispersed-phase viscosity on the simple shear flow of suspensions of two-dimensional liquid drops, *J. Fluid Mech.* **365**, 205 (1998).
6. Jens Eggers, John R. Lister, and Howard A. Stone, Coalescence of liquid drops, *J. Fluid Mech.* **401**, 292 (1999).
7. A. Greenbaum and A. Mayo, Fast parallel iterative solution of Poisson's and the biharmonic equations on irregular regions, *SIAM J. Sci. Stat. Comp.* **13**, 101 (1992).
8. L. Greengard, *The Rapid Evaluation of Potential Fields in Particle Systems* (MIT Press, Cambridge, MA, 1988).
9. Leslie Greengard and Mary Catherine Kropinski, Integral equation methods for Stokes flow in doubly periodic domains, submitted for publication.
10. Leslie Greengard, Mary Catherine Kropinski, and Anita Mayo, Integral equation methods for Stokes flow and isotropic elasticity in the plane, *J. Comput. Phys.* **125**, 403 (1996).

11. L. Greengard and V. Rokhlin, A new version of the fast multipole method for the Laplace equation in three dimensions, *Acta Numerica*, 229 (1997).
12. L. Greengard and V. Rokhlin, Rapid evaluation of potential Fields in three dimensions, in *Vortex Methods*, edited by C. Anderson and C. Greengard Lecture Notes in Mathematics (Springer-Verlag, Berlin/New York, 1988), Vol. 1360.
13. Robert W. Hopper, Plane Stokes flow driven by capillarity on a free surface, *J. Fluid Mech.* **213**, 349 (1990).
14. Thomas Y. Hou, John S. Lowengrub, and Michael J. Shelley, Removing the stiffness from interfacial flows with surface tension, *J. Comput. Phys.* **114**, 312 (1994).
15. S. J. Karrila and S. Kim, Integral equations of the second kind for Stokes flow: Direct solution for physical variables and removal of inherent accuracy limitations, *Chem. Eng. Commun.* **8**, 123 (1989).
16. M. C. A. Kropinski, An efficient numerical method for studying interfacial motion in two-dimensional creeping flows, *J. Comput. Phys.* **171**, 67 (2001).
17. M. C. A. Kropinski, Integral equation methods for particle simulations in creeping flows, *Comput. Math. Appl.* **38**, 67 (1999).
18. W. E. Langlois, *Slow Viscous Flow* (Macmillan Co. New York, 1964).
19. S. Kim and S. J. Karrila, *Microhydrodynamics: Principles and Selected Applications* (Butterworth–Heinemann, Boston, 1991).
20. M. C. A. Kropinski, An efficient numerical method for studying interfacial motion in two-dimensional creeping flows, *J. Comp. Phys.* **171**, 479 (2001).
21. Michael Manga and H. A. Stone, Buoyancy-driven interactions between two deformable viscous drops, *J. Fluid Mech.* **256**, 647 (1993).
22. Michael Manga and H. A. Stone, Collective hydrodynamics of deformable drops and bubbles in dilute low Reynolds number suspensions, *J. Fluid Mech.* **300**, 231 (1995).
23. S. G. Mikhlin, *Integral Equations* (Pergammon, London, 1957).
24. S. G. Muskhelishvili, *Some Basic Problems of the Mathematical Theory of Elasticity* (Noordhoff, Groningen, 1953).
25. V. Z. Parton and P. I. Perlin, *Integral Equation Methods in Elasticity* (MIR, Moscow, 1982).
26. N. Phan-Thien and S. Kim, *Microstructures in Elastic Media* (Oxford Univ. Press, New York, 1994).
27. H. Power, The completed double layer boundary integral equation method for two-dimensional Stokes flow, *IMA J. Appl. Math.* **51**, 123 (1993).
28. H. Power and G. Miranda, Second kind integral equation formulation of Stokes flows past a particle of arbitrary shape, *SIAM J. Appl. Math.* **47**, 689 (1987).
29. C. Pozrikidis, Numerical studies of singularity formation at free surfaces and fluid interfaces in two-dimensional Stokes flow, *J. Fluid Mech.* **331**, 145 (1997).
30. A. R. M. Primo, L. C. Wrobel, and H. Power, An indirect boundary-element method for slow viscous flow in a bounded region containing air bubbles, *J. Eng. Math.* **37**, 305 (2000).
31. S. Richardson, Plane Stokes flows with time-dependent free boundaries in which the fluid occupies a doubly-connected region, *Euro. J. Appl. Math.* **11**, 249 (2000).
32. P. B. Robinson, J. M. Boulton-Stone, and J. R. Blake, Application of the boundary integral method to the interaction of rising two-dimensional deformable gas bubbles, *J. Eng. Math.* **29**, 393 (1995).
33. V. Rokhlin, Rapid solution of integral equations of classical potential theory, *J. Comput. Phys.* **60**, 187 (1985).
34. Y. Saad and M. H. Schultz, GMRES: a generalized minimum residual algorithm for solving nonsymmetric linear systems, *SIAM J. Sci. Stat. Comput.* **7**, 856 (1986).
35. Michael J. Shelley and Tetsuji Ueda, The Stokesian hydrodynamics of flexing, stretching filaments, *Phys. D* **146**, 221 (2000).
36. Saleh Tanveer and Giovani L. Vasconcelos, Time-evolving bubbles in two-dimensional Stokes flow, *J. Fluid Mech.* **301**, 325 (1995).
37. M. Titcombe, M. C. A. Kropinski, and M. J. Ward, A hybrid asymptotic-numerical solution for low Reynolds number flow past an asymmetrical cylindrical body, *Studies Appl. Math.* **105**, 165 (2000).

38. G. A. L. van de Vorst and R. M. M. Mattheij, A BEM-BDF scheme for curvature driven moving Stokes flows, *J. Comput. Phys.* **120**, 1 (1995).
39. G. A. L. van de Vorst, Integral method for a two-dimensional Stokes flow with shrinking holes applied to viscous sintering, *J. Fluid Mech.* **257**, 667 (1993).
40. G. A. L. van de Vorst, Integral formulation to simulate the viscous sintering of a two-dimensional lattice of periodic unit cells, *J. Eng. Math.* **30**, 97 (1996).
41. G. A. L. van de Vorst and R. M. M. Mattheij, Numerical Analysis of a 2-D viscous sintering problem with non-smooth boundaries, *Computing* **49**, 239 (1992).
42. A. Z. Zinchenko and R. H. Davis, An efficient algorithm for hydrodynamical interaction of many deformable drops, *J. Comput. Phys.* **157**, 539 (2000).
43. A. Z. Zinchenko, M. A. Rother, and R. H. Davis, Cusping, capture and breakup of interacting drops by a curvatureless boundary-integral algorithm, *J. Fluid Mech.* **391**, 249 (1999).